Densely packed skyrmions stabilized at zero magnetic field by indirect exchange coupling in multilayers

Fernando Ajejas, Yanis Sassi, William Legrand, Titiksha Srivastava, Sophie Collin, Aymeric Vecchiola, Karim Bouzehouane, Nicolas Reyren, Vincent Cros

Densely packed skyrmions stabilized at zero magnetic field by indirect exchange coupling in multilayers

Fernando Ajejas,[1,*] Yanis Sassi,[1] William Legrand,[1,†] Titiksha Srivastava,[1,‡] Sophie Collin,[1] Aymeric Vecchiola,[1] Karim Bouzehouane,[1] Nicolas Reyren,[1] and Vincent Cros[1,§]

[1]*Unité Mixte de Physique, CNRS, Thales, Université Paris-Saclay, 91767, Palaiseau, France.*

(Dated: May 1, 2023)

Room-temperature stabilization of skyrmions in magnetic multilayered systems results from a fine balance between several magnetic interactions namely symmetric and antisymmetric exchange, dipolar interaction, perpendicular magnetic anisotropy as well as, in most cases, Zeeman through an applied external field. Such field-driven stabilization approach is however not compatible with most of the anticipated skyrmion based applications, e.g. skyrmion memories, logic or neuromorphic computing which motivates a reduction or a cancellation of field requirements. Here we present a method to stabilize at room-temperature and zero-field, a densely packed skyrmion phase in ferromagnetic multilayers with moderate number of repetitions. To this aim, we finely tune the multilayer parameters to stabilize a dense skyrmion phase. Then, relying on the interlayer electronic coupling to an adjacent bias magnetic layer with strong perpendicular magnetic anisotropy and uniform magnetization, we demonstrate the stabilization of sub-60 nm diameter skyrmion at zero-field with adjustable skyrmion density.

Magnetic skyrmions in magnetic heterostructures are non-collinear chiral 2D-like topological spin textures that have attracted great attention in the last decade due to their remarkable properties such as room-temperature (RT) stabilization, small size in the range a few tens of nanometers, current-driven mobility and electrical detection [1–4]. Building on a rapid experimental progress, a variety of devices based on skyrmions have been conceptualized for encoding information, e.g. race track memories, logic devices or neuromorphic computing [5–10]. In order to control the static and dynamical properties of magnetic skyrmions, different material systems have been investigated in order to stabilize different skyrmion configurations going from individual skyrmions to dense skyrmion lattices. Theses skyrmion systems can be ferromagnetic [3, 11–15], ferrimagnetic [16] or more recently 2D materials [17].

In most cases, the application of an external field of at least a few tens of mT is required for the stabilization of a skyrmion phase (SP), as the Zeeman energy is needed for the transition from the topologically trivial maze-domain configuration at zero-field. Nonetheless, in addition to the simple use of an external field, other approaches have been proposed for nucleation or stabilization of skyrmions such as current induced nucleation [3, 4, 18], irradiation [19], probe interaction [20, 21], X-ray illumination [22], ultrafast laser pulses [23] or artificial defects created by lithography [24, 25] among others.

From a practical point of view, the precise control of the external field allows to finely tune the skyrmion size as well as the density [15, 26]. On a more fundamental aspect, Büttner *et al.* [27] recently investigated the formation process of skyrmion lattices at pico-second time scale by combining an ultrashort laser pulse together with a static external magnetic field, that is required to break the time-reversal symmetry. Hence, beyond the fact that it may be an obstacle for the application of skyrmions in new types of computing devices, the use of an external field can also be complication to address experimentally some still-debated questions about the actual skyrmion nucleation mechanisms and their time scale [28]. To tackle this limitation, the stabilization of magnetic textures without any external field still remains an important challenge. Indeed, isolated skyrmions or skyrmionic bubbles in ferromagnetic multilayers (MML) have been already successfully stabilized at zero-field either in confined structures [13], using the interlayer exchange interaction from a perpendicularly magnetized single films [29, 30] or magnetic field history [18, 31–33]. Note that for some applications, such as reservoir or neuromorphic computing fields [34–36], there is a clear advantage of working with dense skyrmion ensembles instead of isolated skyrmions.

In this study, we demonstrate that zero external magnetic field (zero-field) SP can be stabilized at RT. To this aim, we first investigate the dependence of the skyrmion size and density on different parameters of the magnetic multilayers. The first objective is to reduce the field required for the SP stabilization down to a few tens of mT. Then we describe the approach developed to stabilize zero-field SP in multilayers relying on an indirect exchange interaction generated by an additional bias layer with uniform perpendicular magnetization. The effective magnetic field created by the bias layer is electronically coupled to the skyrmion magnetic multilayers through a non-magnetic (NM) layer replacing the external field in stabilizing the SP. We demonstrate using magnetic force microscopy (MFM) the stabilization of zero-field SP with skyrmion diameter as small as 60 nm. Moreover, besides the small skyrmion size, we demonstrate that their density can be easily controlled by finely tuning the thicknesses of both ferromagnetic (FM) and NM layers, which is not the case for all the other approaches for having zero-field stabilization.

The magnetic multilayers have been grown by dc magnetron sputtering on thermally oxidized silicon wafers with 280 nm of SiO_2, under 0.25 mbar dynamic Ar pressure (base pressure is 7×10^{-8} mbar). All the samples have a bottom buffer layer made of Ta(5)|Pt(8) and capped with 3 nm Pt layer to prevent oxidation, as schematized in Fig. 1(a). Alternating

gradient field magnetometer (AGFM) and SQUID are used to measure the anisotropy field H_K, and the spontaneous magnetization M_s. Magnetic imaging using MFM has been performed with low-moment magnetic tips in double pass tapping mode-lift mode. A custom made magnetic tip coated with a 7-nm thick CoFeB layer has been used for its low magnetic moment in order to limit the perturbation of the magnetic textures in the SP. The MFM setup is equipped with a variable external field module which allows us to modify the external field on demand between two different measurements. The scanned area remains the same regardless small drifts due to the external field and small temperature variations.

The stabilization of the skyrmion configuration and its final characteristics is governed by the balance between the different magnetic energies, i.e., the direct Heisenberg exchange constant (A), the Dzyaloshinskii-Moriya interaction (DMI), the magnetic uniaxial anisotropy (K_u) and the dipolar energies, necessitating a precise magnetic characterization of the samples. The effective interfacial DMI (D_{eff}) as function of the thickness ($D_s = D_{eff} t_{Co}$) has been measured by k-resolved BLS to be $D_s = -1.27$ pJ/m [37, 38]. We notice that, even if the Pt thickness is only 0.6 nm, it results in an effective perpendicular anisotropy (PMA) and an amplitude of the DMI close to the value of thick layers ($\simeq 3$ nm), as we previously demonstrated in Ref. [38]. The thickness of Ru of 1.4 nm leads to a ferromagnetic RKKY interaction between two consecutive Co layers [39]. In recent work, we found that the exchange constant A depends on the FM thickness in the range that we consider here. This parameter is taken to be equal to $A = 23$ pJ/m from [38].

In order to characterize the magnetic properties of the MML as a function of t_{Co}, we grew a series of samples with $n = 10$ varying t_{Co} from 0.6 to 1.9 nm. A schematic view of the studied multilayers composed of a trilayer of (Pt(0.6)|Co(t_{Co})|Ru(1.4)) repeated n times is shown in Fig. 1(a) (numbers in parentheses indicate the thickness of each layer in nm). Through the out-of-plane hysteresis loops shown in Fig. 1(b) together with in-plane hysteresis loops (Fig. S1), the important magnetic parameters can be determined, namely the saturation magnetization (M_s), the out-of-plane (H_{sat}) and in-plane (H_K) saturation fields , the effective (K_{eff}) and uniaxial anisotropies (K_u) and the skyrmion density (ρ_{sk}) and diameter (D_{sk}) measured from the MFM image. Their evolutions with t_{Co} are shown in Fig. 1(c-h). The saturation magnetization $M_s t_{Co}$ [Fig. 1(c)] displays a quasi-linear increase with t_{Co}. Note that a null magnetization is extrapolated for finite $t_{Co} \approx 0.4$ nm, suggesting that, for this thickness, the Curie temperature (T_c) is below RT, similarly to what has been found for similar magnetic trilayers (see Ref. [40]). The slope indicates the intrinsic $M_s = 1.56 \pm 0.01$ MA/m, a value close to the bulk Co M_s value. The saturation field H_{sat} displayed in Fig. 1(d) with black open dots shows a continuous increment as a function of t_{Co}, with a marked increase above 1.4 nm. The in-plane saturation field H_K represented with open blue dots decreases from 0.8 nm crossing H_{sat} at 1.6 nm, suggesting the spin reorientation transition (SRT) from out-of-plane to in-plane.

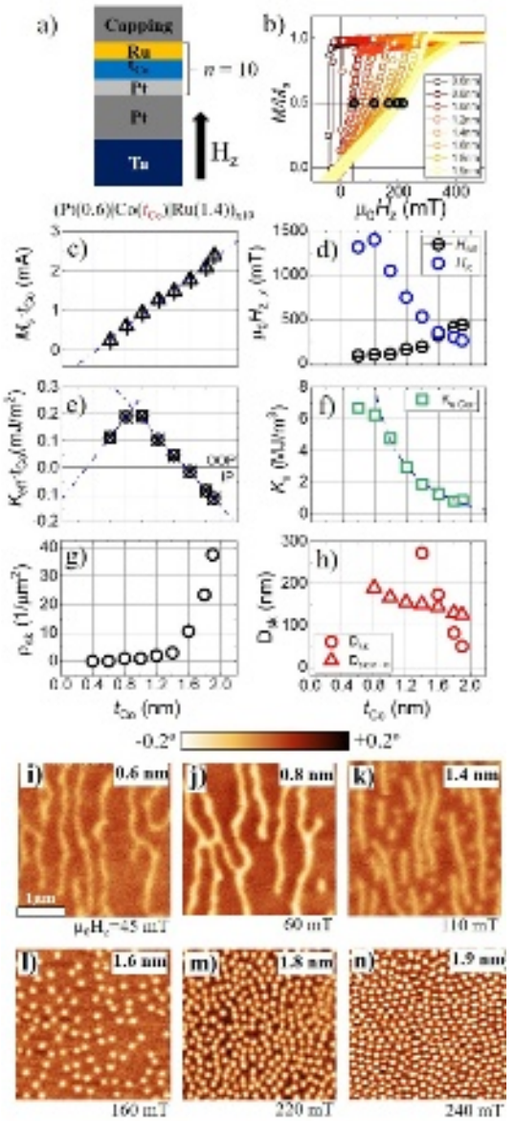

FIG. 1. a) Scheme of MML (Pt|Co(t_{Co})|Ru)$_{\times n}$, t_{Co} is cobalt thickness, n number of repetitions, and H_z the applied perpendicular field; b) Room temperature out-of-plane hysteresis loops of (Pt|Co(t_{Co})|Ru)$_{\times 10}$ for a t_{Co} ranging from 0.6 to 1.9 nm. Black circles indicate the points at which MFM images shown in (i, j, k, l, m, n) were taken; c-h) Magnetic parameters as function of t_{Co}: c) magnetization at saturation M_s multiplied by the nominal Co thickness (dotted blue line is a linear fit), d) out-of-plane H_{sat} (black circles) and in-plane H_K (blue circles) saturation fields, e) effective anisotropy energy K_{eff} (lines described in the text), f) corrected uniaxial anisotropy energy $K_{u\,Corr}$ (blue dotted line described in the text), g) Skyrmion density, ρ_{sk} and h) skyrmion apparent diameter D_{sk} calculated from ρ_{sk} and mean magnetization (red circles) and extracted from MFM (red open triangles). i-n) Room-temperature MFM images at $H_{z|<M>=M_s/2}$) for $t_{Co} = 0.6$ nm (i), 0.8 nm (j), 1.4 nm (k), 1.6 nm (l), 1.8 nm (m) and 1.9 nm (n).

We then study the evolution of the effective anisotropy

$K_{\rm eff}$ extracted from $\mu_0 H_K = 2K_{\rm eff}/M_{\rm s}$. This value is multiplied by Co thickness ($K_{\rm eff} t_{\rm Co}$) to be represented as a function of $t_{\rm Co}$ in Fig. 1(e). From $t_{\rm Co}$ = 0.6 to 1.0 nm, $K_{\rm eff} t_{\rm Co}$ first increases reaching the maximum value around $t_{\rm Co}$ = 0.9−1 nm. Thereafter $K_{\rm eff} t_{\rm Co}$ decreases linearly up to the largest Co thickness. We find the SRT from out-of-plane to in-plane ($K_{\rm eff}$ = 0) at $t_{\rm Co}$ = 1.53 nm, in good agreement with other series of $({\rm Pt|Co|Ru})_{\times n}$ that we studied recently [38, 39]. The linear fit in Fig.1(e) (blue line) is expected to have a slope equal to $-\mu_0 M_s^2/2$ in the equation considering the shape anisotropy and a purely interfacial PMA only. The estimated value is in fact not compatible with the value of M_s deduced from Fig. 1(c), indicating that an additional component is needed, to explain the data in panel (e). Similarly, the calculated $K_{\rm u} = K_{\rm eff} + \mu_0 M_s^2/2$ is not constant. Therefore, we need to consider the existence of a magnetocrystalline anisotropy constant $K_{\rm u,c}$. The linear fit in Fig.1(e) suggests $K_{\rm u,c} = -1.9 \pm 0.1$ MJ/m^3 and $K_{\rm u,s} = 3.8 \pm 0.1$ mJ/m^2. The corrected $K_{\rm u}$ ($K_{\rm u\,Corr}$) is represented with open squares in Fig. 1(h). The fitting dashed blue line corresponds to the expression $K_{\rm u,s}/t_{\rm Co} + K_{\rm u,c}$. We analyze the evolution of the magnetic configuration as function of $t_{\rm Co}$ under external field. In Fig. 1(i-n) are shown the MFM images corresponding to $t_{\rm Co}$ = 0.6, 0.8, 1.4, 1.6, 1.8 and 1.9 nm respectively. The objective is to determine $t_{\rm Co}$ allowing to turn the stripe domains into a densely packed skyrmion configuration at intermediate state in the magnetization loop ($< m_z > = 0.5$). For larger and moderate (but still positive) $K_{\rm eff}$ values, we find that only stripe domains or a combination of isolated skyrmions together with meander domains are stabilized [see Fig. 1(i-j)] respectively. The SP can be stabilized at thicknesses smaller than the SRT with slightly positive $K_{\rm eff}$ (1.4 nm). However, large Zeeman energy is required to reach a SP, hence requiring field values near saturation. For $< m_z > = 0.5$, a moderate number of skyrmions combined with domains is visible in Fig. 1(k). Above SRT (i.e. $K_{\rm eff} < 0$), the stabilization of SP at $< m_z > = 0.5$ is possible as shown in Fig. 1(l). The thicker the FM layer is, the higher is the ordering and the density [Fig. 1(m-n)] for $t_{\rm Co}$ =1.8 nm and 1.9 nm respectively. The density is analyzed from Fig. 1(g) finding that it increases exponentially up to 40 ±2 sky/μm^{-2} in agreement with [41].

In order to determine the evolution of $D_{\rm sk}$, we estimate their actual value from $\rho_{\rm sk}$ and the m_z value obtained in the hysteresis loop at the same field that the one used for the MFM images, i.e., $D_{\rm sk} \approx \sqrt{2(1-m_z)/(\pi \rho_{\rm sk})}$ [open red dots in Fig. 1(h)]. Following this approach, the $D_{\rm sk}$ is found to decrease by 80% from $t_{\rm Co}$ =1.4 nm to 1.9 nm. A second method to estimate the skyrmion diameter is to measure the full width at half maximum (FWHM) of the corresponding skyrmions from MFM phase signal. The results are shown with red triangles in Fig. 1(h), presenting for both methods, the same trend with a decrease with $t_{\rm Co}$ but less accentuated for the first one (20%). From this analysis, we select $t_{\rm Co}$ = 1.6 nm and $n = 10$ as it is the best compromise between order, density of the SP and the external field requirements at $< m_z > = 0.5$.

Our objective is to optimize the stabilization of the SP and to minimize the required external field. To achieve this, we analyze the impact of the number of repetitions and the thickness of the lower Pt layer on the saturation field, the dipolar fields and the anisotropy. By considering these factors, we can determine the effect on the $\rho_{\rm sk}$ or $D_{\rm sk}$ of the SP. While increasing the number of repetitions increases thermal stability and signal-to-noise ratio, we find that it also implies an increase of the external field that will be needed to stabilize the skyrmions [42]. As $< m_z > = 0.5$ is proportional to the out-of-plane saturation field, we study the variation of $H_{\rm sat}$ together wit H_K extracted from the out and in-plane hysteresis loops in different multilayers with $n = 1$ to $n = 20$ repetitions (Fig. S2). As shown in Fig. 2(a), $H_{\rm sat}$ follows approximately a linear evolution up to $n = 12$, above which it remains constant. However, H_K shows a continuous linear increase without saturation, leading to an enhancement in both $K_{\rm eff}$ and $K_{\rm u}$ values [Fig. 2(b)]. For a number of repetitions larger than 10, $K_{\rm eff}$ becomes positive increasing from -0.009 to 0.5 MJm-3. Similarly $K_{\rm u}$ increases from 0.36 to 5 MJm-3. In Fig. 2(e-h), we display the MFM images with n = 3, 5, 10, 15 and 20 as function of the minimum applied external magnetic field $\mu_0 H_z$ allowing the observation of the transition from labyrinth configuration into a SP, determining $\rho_{\rm sk}$ and $D_{\rm sk}$. The result of the quantitative analysis is presented in Fig. 2(c), showing a monotonic increase (40%) of the $\rho_{\rm sk}$ from n = 10 to 20. After studying the trend for the skyrmion diameter, it becomes apparent that the two methods exhibit contrasting trends. $D_{\rm skMFM}$ displays an upward trend with increasing n, that is consistent with Ref. [32]. Both measurements intersect after n =10 pointing to a dominant role of dipole fields and in-plane fields effects for samples with more than n =10. Following the results presented before, we will choose $n = 3$ for the rest of the study, as being the best compromise between the impact of the interlayer dipolar fields and a good thermal stability. Thus, we can stabilize a dense SP with an external field that is four times smaller than for the sample with $n = 20$.

For this number of repetitions, $H_{\rm sat}$ can then be further reduced by decreasing the dipolar fields through the increase of the interlayer thickness of the NM layers. As shown Fig. 2(i), we find a $1/t_{\rm tot}$ reduction of $H_{\rm sat}$ as function of the Pt thickness ($t_{\rm Pt}$) ranging from 0.6 to 8 nm, $t_{\rm tot}$ being the total trilayer thickness. In this case H_K remains almost constant. So for thicknesses greater than 1nm both $K_{\rm eff}$ and $K_{\rm u}$ remain constant [Fig. 2(i)] even if the Pt layer is increased up to 8 nm. (In Fig. S3 are shown the IP hysteresis loops confirming identical anisotropy values from $t_{\rm Pt}$ = 0.6 to 8 nm). In Fig. 2(m-o), we present the MFM images showing a SP configuration for $t_{\rm Pt}$ = 3, 5 and 8 nm. Even though the reduction of the external field is about 60% between $t_{\rm Pt}$ = 3 and 8 nm, both $\rho_{\rm sk}$ and $D_{\rm skMFM}$ extracted from the MFM images are found not to change significantly [see Fig. 2(k-l)]. Note however that determining $D_{\rm sk}$ from the m_z and $\rho_{\rm sk}$, the diameter increases by more than 50 % when the Pt spacer layer increases from 0.6 to 8 nm [see open circles in Fig. 2(l)]. This suggests that the two methods differ more when the dipole fields are smaller i.e. for

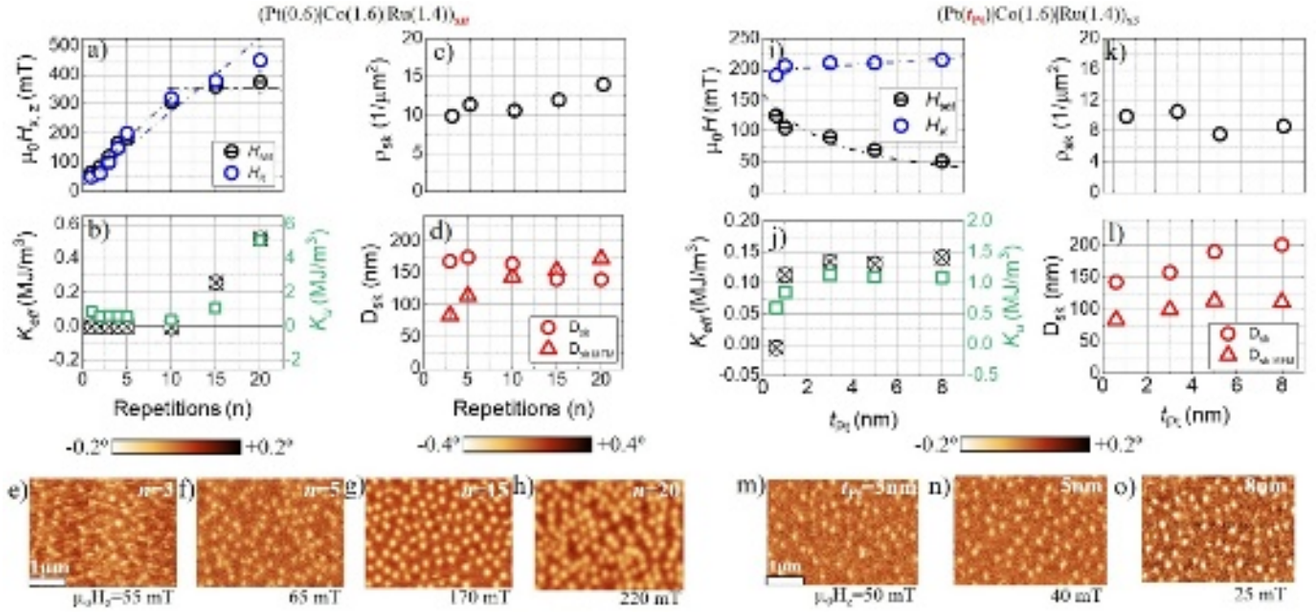

FIG. 2. a) H_{sat} (black circles) and H_K (blue circles) as function of the number of repetitions n of $(Pt(0.6)|Co(1.6)|Ru(1.4))_{\times n}$ multilayer. The black dashed lines are guides for the eyes, blue dashed line is a linear fit. b) Effective K_{eff} and uniaxial K_u anisotropy (right axis) as function of n. c) Skyrmion density, ρ_{sk}, d) skyrmion apparent diameter D_{sk} calculated from ρ_{sk} and mean magnetization (red circles) and extracted from MFM (red open triangles) as function of the number of repetitions n. e-h) MFM images of SP of systems with $n = 3$ (e), $n = 5$ (f), $n = 15$ (g), $n = 20$ (h). i) H_{sat} (black circles) and H_K (blue circles) vs. Pt thickness (t_{Pt}) in $(Pt(t_{Pt})|Co(1.6)|Ru(1.4))_{x3}$ multilayer. H_{sat} is adjusted with $1/t$ fit. j) Effective K_{eff} and uniaxial K_u anisotropy (right axis) as function of t_{Pt} k) Skyrmion density, ρ_{sk}, l) skyrmion apparent diameter D_{sk} calculated from ρ_{sk} and mean magnetization (red circles) and extracted from MFM (red open triangles) as function of t_{Pt}. m-o) MFM images of SP of systems with t_{Pt} = 3 nm (c), t_{Pt} = 5 nm (d) and t_{Pt} = 8 nm (e).

samples with lower number of repetitions. Then, we decide to use the following stacking sequence for the skyrmion MML: $(Pt(8)|Co(1.6)|Ru(1.4))_{\times 3}$.

Thanks to the previously described optimization of the MML properties, we find that a densely packed SP can be stabilized at relatively low external field values. We can thus envisage to replace such external field by a bias field generated by interlayer electronic coupling generated inside the MML by adding some uniformly magnetized layers. In Fig. 3(a), a schematic view of the complete sample allowing the zero-field stabilization of SP is presented. In addition to the already designed Pt|Co|Ru multilayered stack that hosts the skyrmions, it is composed of a bias layer (BL) grown on the the buffer layer (Ta|Pt) and a NM spacer Pt coupling layer (CL) through which the indirect exchange coupling is modulated. We show here how the properties of the BL and CL may be engineered. We first optimize the BL aiming at reaching a strong enough effective field (H_{eff}^{bias}) needed to stabilize the SP. The first important characteristic of the BL is that it should have a large PMA together with a completely uniform magnetization at remanence. The hysteresis loop of the BL composed of $(Pt(0.4)|Co(0.6))_{\times 4}$ is presented as the black open dots curve in Fig. 3(b). Note that we have chosen this final composition after having studied the BL properties as a function of the number of repetitions (see Fig. S4(a)) showing squared shape with sharp transitions. The actual amplitude of H_{eff}^{bias} has been experimentally estimated following the procedure that we developed in Ref. [39]. Further information can be found in Fig. S4(c-d) of the Supplementary Material. The next step is to optimize the thickness of the CL through which the BL is electronically coupled to the skyrmion MML. We know from the previous section that the H_{eff} amplitude required to stabilize the SP is ≈ 25 mT. The CL thickness determines directly the amplitude of the effective bias field H_{eff}^{bias} acting on the bottom of the skyrmion MML. The evolution of H_{eff}^{bias} as function of t_{Pt}^{bias} coupling layer is presented in Fig. 3(c), in which we see that H_{eff}^{bias} decays exponentially, almost vanishing at $t_{Pt}^{bias} = 3$ nm. Note that the choice of the CL thickness influences indeed also the magnetization reversal process of the complete MML system. For example, we find that for $t_{Pt}^{bias} < 2.2$ nm, the effective field H_{eff}^{bias} is too large, making that the BL and the skyrmion multilayer are sufficiently coupled, so that their magnetizations reverse simultaneously, hence no skyrmion can be stabilized. In the inset of Fig. 3(c), we display the experimental results showing H_{eff}^{bias} vs H_z^{switch}. We define H_z^{switch} as the external field applied when the BL magnetization switching reversal occurs. The interesting coupling regime is when the BL and the skyrmion MML switch independently, keeping a large enough bias field. It corresponds to t_{Pt}^{bias} ranging from 2.2 to 3.0 nm. More details about the reversal mechanisms can be found in Fig. S4(b), where the loops are labeled with arrows pointing at H_z^{switch}. The hysteresis

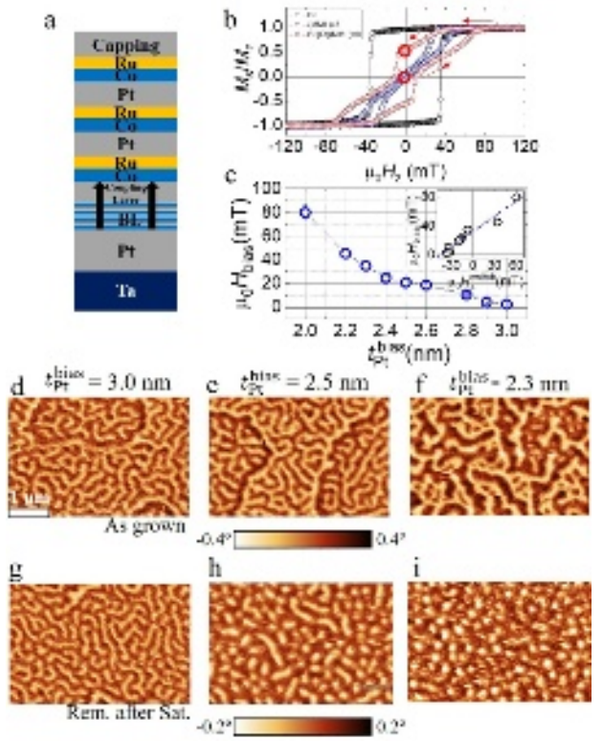

FIG. 3. a) Sketch of BL|Pt(t_{Pt})|MML. BL is the bias-layer with stacking: $(Pt(0.45)|Co(0.6))_{x4}$, t_{Pt} the Pt coupling-layer thickness and MML the multilayer hosting SP $(Pt(8)|Co(1.6)|Ru(1.4))_{x3}$. b) AGFM out-of-plane hysteresis loops of BL (black), MML (blue) and BL|Pt(2.3)|MML (red). c) Effective bias field ($\mu_0 H_{bias}$) as function of Pt coupling-layer (t_{Pt}). The inset is $\mu_0 H_{bias}$ vs switching field ($\mu_0 H_{switch}$). d-i) MFM images of as grown remanence after saturation state for Pt coupling-layer thickness t_{Pt}=3.0 nm (d, g), t_{Pt}=2.5 nm (e, h), t_{Pt}=2.3 nm (f, i).

loop of the complete system with a CL of $t_{Pt}^{bias} = 2.3$ nm is displayed with red circles in Fig. 3(b), where the blue dot curve is the loop of the skyrmion MML. The experimental procedure to prepare magnetically the system leading to the zero-field stabilization of SP consist first in a complete saturation of the MML magnetization followed by sweeping the external field back to zero [red arrows in Fig. 3(b)]. Red circles are initial and final magnetization state.

In Fig. 3 are presented the MFM images of the as-grown magnetization state (d-f) and at remanence after saturation (g-i) for three CL thickness, t_{Pt}^{bias} = 3.0, 2.5 and 2.3 nm. First, we see that in the as-grown state, some large domains ($\approx \mu$m size) are present in the BL coexisting with smaller labyrinthine domains from the skyrmion MML. On the contrary, after having saturated the system applying $H_z \geq 80$ mT and returning to remanence (see Fig.3 (g-i)), the bias layer magentization remains monodomain and only the magnetic configuration from the skyrmion MML is detected by MFM. For $t_{Pt}^{bias} = 3.0$ nm, the remnant structure consists of a maze-domain configuration (see Fig. 3(g)). For t_{Pt}^{bias} = 2.5 nm, the magnetic configuration is mainly composed of skyrmions together with elongated domains (see Fig. 3(h)). Finally, for $t_{Pt}^{bias} = 2.3$ nm presented in Fig. 3(i), the MFM image clearly indicates that the zero-field SP is stabilized.

In this part, we aim at investigating how ρ_{sk} and D_{sk} can be adjusted by finely tuning various MML parameters. Beginning with the optimized system described above, i.e., BL|Pt(2.3)|$[Pt(8)|Co(1.6)|Ru(1.4)]_{\times 3}$ we can slightly modify anisotropies and dipolar fields in two ways: i) by increasing t_{Co} using the system BL|Pt(2.3)|$[Co(1.7)|Ru(1.4)|Pt(8)]_{\times 3}$, and ii) by reducing the distance of the FM layers varying the NM bottom layer thickness of the trilayer from 8 to 5 nm. This yields the experimental system BL|Pt(2.3)|$[Co(1.6)|Ru(1.4)|Pt(5)]_{\times 3}$. We first analyze the zero-field SP's statistics of the optimized sample. In Fig. 4(a), we present the corresponding MFM image, while the distribution of the number of skyrmions as a function of D_{skMFM} is shown in Fig. 4(b). The diameter distribution can be accurately fitted with a Gaussian function, resulting in a mean diameter of 85 ± 5 nm. Based on the analysis of a $5 \times 5\,\mu m^2$ MFM image, the density is found to be $10\,\mu m^{-2}$, slightly higher but in agreement with same system without the BL. In Fig. 4(c), we display the resulting SP imaged by MFM at zero field after saturation for the sample with $t_{Co} = 1.7$ nm. As expected, the correspondingly modified anisotropies and interlayer dipolar fields leads to a different characteristics of the zero-field SP. The $D_{sk,MFM}$ distribution in Fig. 4(d) can be fitted with a Gaussian function with mean diameter $\approx 90 \pm 5$ nm and with a density of $7.0\,\mu m^{-2}$. Note that there is a reduction of about 30% of ρ_{sk} by increasing t_{Co} 0.1 nm (6%). Finally, in Fig. 4(e) is shown the MFM image of the system with $t_{Pt} = 5$ nm. Note that for this sample, we had to use a lower magnetization tip to measure without no apparent disruption of the magnetic configuration, leading to a much lower MFM contrast. In this case, the D_{skMFM} distribution is fitted with an asymmetric Lorentz 2σ function presenting a mean diameter 60 ± 5 nm and a density of $12\,\mu m^{-2}$, leading to a reduction of the apparent MFM radius of almost 30%. Note that using 5 nm thickness of NM bottom layer, the required BL H_{eff}^{bias} is larger than the one for 8 nm [Fig.2(n-o)], hence there are a few remaining wormy-like domains.

Finally, we discuss the role of the BL on the skyrmion characteristics. ρ_{sk} and D_{sk} have related to κ that is the critical parameter describing the skyrmion stability ($\kappa = \pi D/4\sqrt{AK_{eff}}$) [15, 43, 44]. Using the values that have determined experimentally, we calculate that κ parameter ranges between 0.2 and 0.35 at the maximum. These relatively low values seems to indicate that the SP should be considered as configuration with a large density of isolated skyrmions rather than a real skyrmion lattice phase, that is expected only for κ larger than 1. Note however, that if K_{eff} is used in the κ calculations instead of K_u, as done often, such estimation of κ cannot be done in case $K_{eff} < 0$. The behavior of ρ_{sk} and D_{sk} with respect to K_u are represented in Fig. 4(g) and (h) respectively. The general trends for ρ_{sk} and D_{sk} following a negative slope are in good agreement with results found by

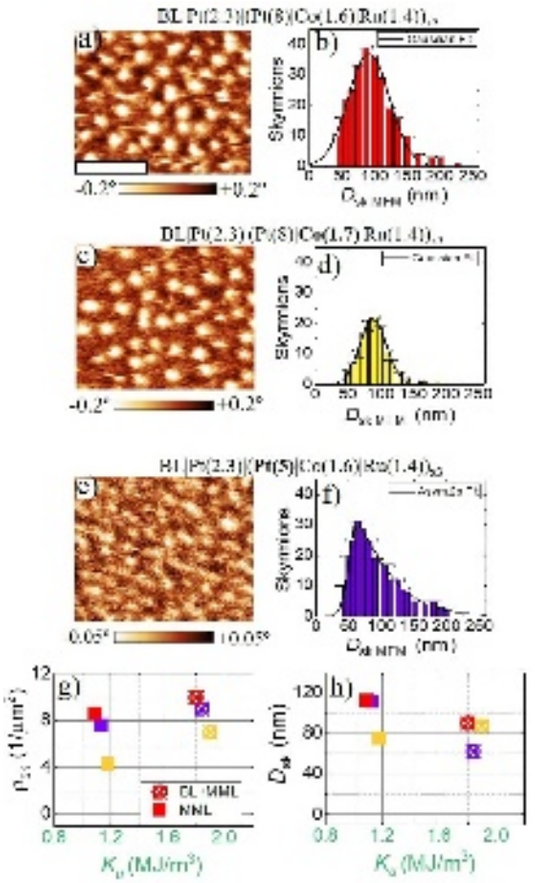

FIG. 4. (a) BL|Pt(2.3)|[Co(1.6)|Ru(1.4)|Pt(8)]$_{\times 3}$ sample. MFM image of zero-field SP at remanence after saturation. (b) Corresponding number of skyrmions distribution as function of $D_{\mathrm{sk,FWHM}}$ extracted by MFM image analysis. Black line is a Gaussian fit. (c) BL|Pt(2.3)|[Co(1.7)|Ru(1.4)|Pt(8)]$_{\times 3}$ sample. MFM image of zero-field SP at remanence after saturation. (d) Corresponding number of skyrmions distribution as function of $D_{\mathrm{sk,FWHM}}$ extracted by MFM image analysis. Black line is a Gaussian fit. (e) BL|Pt(2.3)|[Co(1.6)|Ru(1.4)|Pt(5)]$_{\times 3}$ sample. MFM image of zero-field SP at remanence after saturation. (f) Corresponding number of skyrmions distribution as function of $D_{\mathrm{sk,FWHM}}$ extracted by MFM image analysis. Black line is an asymmetric Lorentz 2σ function fit. g) skyrmion density ρ_{sk} and h) skyrmion apparent diameterD_{sk} as function of K_{u} of BL+MML samples (open circles and MML (filled squares).

other groups [41, 42]. However all the points associated to BL+MML (open symbols) are shifted towards larger values, being K_{u} more than double. This indicates a potential increase of the effective anisotropy because of the coupling with the BL. The optimized BL+MML sample (open red circles) has a similar density than the MML (red squares), however showing a smaller D_{skMFM}. The sample with $t_{\mathrm{Co}} = 1.7$ nm (yellow) presents different behavior with and without BL. The MML is fully in-plane ($K_{\mathrm{eff}} < 0$), and having only 3 repetitions, few skyrmions are stabilized. However, in presence of the BL, the skyrmion density is double. Another interesting result is that the $D_{\mathrm{sk\,MFM}}$ does not decrease compared to the optimized sample. This could indicates that the anisotropy induced by BL plays an important role in the minimum energetic state of the skyrmions at remanence. Similar results are observed for sample with $t_{\mathrm{Pt}} = 5$ nm. (purple), the resulting ρ_{sk} follows MML behavior, however is the $D_{\mathrm{sk\,MFM}}$ where the difference is more accentuated with a large decrease. This fact, together with the asymmetric fit in the distribution of radii, indicates a large variation in the remnant energetic state due to the BL.

In conclusion, we thoroughly explore how to stabilize a densely packed skyrmion phase in a MML without requiring an external magnetic field. We describe how by adjusting the properties of the magnetic layers in the MML $(\mathrm{Pt}(t_{\mathrm{Pt}})|\mathrm{Co}(t_{\mathrm{Co}})|\mathrm{Ru}1.4)_{\times n}$, with a moderate number of repetitions, specifically $n = 3$ and a larger $t_{\mathrm{Pt}} = 8$ nm, we are able to precisely control the size and density of the skyrmion phase at zero field. This is achieved by generating an effective magnetic field via an electronically coupled, uniformly magnetized bias layer, which effectively transforms the labyrinthine domain configuration into a dense skyrmion phase configuration. By slightly varying the thickness of the trilayer, the skyrmion diameter and density can be tuned, leading to a variation of the $H_{\mathrm{eff}}^{\mathrm{dip}}$. Such precise control of ρ_{sk} and D_{sk} at zero field is an important outcome of this work and could for example facilitate the investigation of fundamental mechanisms and the time-scale required to overcome the topological barrier leading to the nucleation of a skyrmion phase. The presented approach might also present some compelling opportunities for neuromorphic computing applications based on skyrmion phase-based systems.

In the supplementary material are presented all the hysteresis loops of the experimental samples, additional MFM images and explanations for the quantification of the bias field.

This work has been supported by DARPA TEE program grant ($MIPRHR - 0011831554$), by ANR agnecy as part of the "Investissements d'Avenir" program (Labex NanoSaclay, reference: ANR-10-LABX-0035, the FLAG-ERA Sograph-MEM (ANR-15-GRFL-0005) and the Horizon2020 Framework Program of the European Commission, under FET-Proactive Grant agreement No. 824123 (SKYTOP).

* fajejas@physics.ucsd.edu; Current address: Department of Physics and Center for Advanced Nanoscience, University of California, San Diego La Jolla, CA, 92093, USA.
† Current address: Department of Materials, ETH Zürich, CH-8093 Zürich, Switzerland .
‡ Current address: SPEC, CEA, CNRS, Université Paris-Saclay, 91191, Gif-sur-Yvette, France.
§ vincent.cros@cnrs-thales.fr

[1] A. Fert, V. Cros, and J. Sampaio, Nature nanotechnology **8**, 152 (2013).
[2] R. R. M. Everschor-Sitte K., Masell J. and M. Kläui, Journal of Applied Physics **124**, 240901 (2018).
[3] W. Jiang, P. Upadhyaya, W. Zhang, G. Yu, M. B. Jungfleisch, F. Y. Fradin, J. E. Pearson, Y. Tserkovnyak, K. L. Wang,

O. Heinonen, et al., Science **349**, 283 (2015).
[4] M. He, L. Peng, Z. Zhu, G. Li, J. Cai, J. Li, H. Wei, L. Gu, S. Wang, T. Zhao, B. Shen, and Y. Zhang, Applied Physics Letters **111**, 202403 (2017).
[5] A. Fert, N. Reyren, and V. Cros, Nature Reviews Materials **2**, 17031 (2017).
[6] R. Tomasello, E. Martinez, R. Zivieri, L. Torres, M. Carpentieri, and G. Finocchio, Scientific reports **4**, 1 (2014).
[7] G. Finocchio, F. Buettner, R. Tomasello, M. Carpentieri, and M. Kläui, Journal of Physics D: Applied Physics **49**, 423001 (2016).
[8] M. Chauwin, X. Hu, F. Garcia-Sanchez, N. Betrabet, A. Paler, C. Moutafis, and J. S. Friedman, Physical Review Applied **12**, 064053 (2019).
[9] E. Y. Vedmedenko, R. K. Kawakami, D. D. Sheka, P. Gambardella, A. Kirilyuk, A. Hirohata, C. Binek, O. Chubykalo-Fesenko, S. Sanvito, B. J. Kirby, et al., Journal of Physics D: Applied Physics **53**, 453001 (2020).
[10] S. Li, W. Kang, X. Zhang, T. Nie, Y. Zhou, K. L. Wang, and W. Zhao, Mater. Horiz. **8**, 854 (2021).
[11] N. Romming, C. Hanneken, M. Menzel, J. E. Bickel, B. Wolter, K. von Bergmann, A. Kubetzka, and R. Wiesendanger, Science **341**, 636 (2013).
[12] C. Moreau-Luchaire, C. Moutafis, N. Reyren, J. Sampaio, C. A. F. Vaz, N. Van Horne, K. Bouzehouane, K. Garcia, C. Deranlot, P. Warnicke, P. Wohlhüter, J.-M. George, M. Weigand, J. Raabe, V. Cros, and A. Fert, Nature Nanotechnology **11**, 444 (2016).
[13] O. Boulle, J. Vogel, H. Yang, S. Pizzini, D. de Souza Chaves, A. Locatelli, T. O. Menteş, A. Sala, L. D. Buda-Prejbeanu, O. Klein, et al., Nature nanotechnology **11**, 449 (2016).
[14] S. Woo, K. Litzius, B. Krüger, M.-Y. Im, L. Caretta, K. Richter, M. Mann, A. Krone, R. M. Reeve, M. Weigand, P. Agrawal, I. Lemesh, M.-A. Mawass, P. Fischer, M. Kläui, and G. S. D. Beach, Nature Materials **15**, 501 (2016).
[15] A. Soumyanarayanan, M. Raju, A. Gonzalez Oyarce, A. K. Tan, M.-Y. Im, A. Petrović, P. Ho, K. Khoo, M. Tran, C. Gan, et al., Nature materials **16**, 898 (2017).
[16] L. Caretta, M. Mann, F. Buettner, K. Ueda, B. Pfau, C. M. Guenther, P. Hessing, A. Churikova, C. Klose, M. Schneider, D. Engel, C. Marcus, D. Bono, K. Bagschik, S. Eisebitt, and G. S. D. Beach, Nature Nanotechnology **13**, 1154 (2018).
[17] Y. Wu, S. Zhang, J. Zhang, W. Wang, Y. L. Zhu, J. Hu, G. Yin, K. Wong, C. Fang, C. Wan, et al., Nature communications **11**, 1 (2020).
[18] S. Mallick, S. Panigrahy, G. Pradhan, and S. Rohart, Phys. Rev. Appl. **18**, 064072 (2022).
[19] K. Fallon, S. Hughes, K. Zeissler, W. Legrand, F. Ajejas, D. Maccariello, S. McFadzean, W. Smith, D. McGrouther, S. Collin, et al., Small **16**, 1907450 (2020).
[20] S. Zhang, J. Zhang, Q. Zhang, C. Barton, V. Neu, Y. Zhao, Z. Hou, Y. Wen, C. Gong, O. Kazakova, et al., Applied Physics Letters **112**, 132405 (2018).
[21] A. Ognev, A. Kolesnikov, Y. J. Kim, I. H. Cha, A. Sadovnikov, S. Nikitov, I. Soldatov, A. Talapatra, J. Mohanty, M. Mruczkiewicz, et al., ACS nano **14**, 14960 (2020).
[22] Y. Guang, I. Bykova, Y. Liu, G. Yu, E. Goering, M. Weigand, J. Gräfe, S. K. Kim, J. Zhang, H. Zhang, Z. Yan, C. Wan, J. Feng, X. Wang, C. Guo, H. Wei, Y. Peng, Y. Tserkovnyak, X. Han, and G. Schütz, Nature Communications **11**, 949 (2020).
[23] S.-G. Je, P. Vallobra, T. Srivastava, J.-C. Rojas-Sánchez, T. H. Pham, M. Hehn, G. Malinowski, C. Baraduc, S. Auffret, G. Gaudin, S. Mangin, H. Béa, and O. Boulle, Nano Letters **18**, 7362 (2018), pMID: 30295499, https://doi.org/10.1021/acs.nanolett.8b03653.
[24] B. F. Miao, L. Sun, Y. W. Wu, X. D. Tao, X. Xiong, Y. Wen, R. X. Cao, P. Wang, D. Wu, Q. F. Zhan, B. You, J. Du, R. W. Li, and H. F. Ding, Phys. Rev. B **90**, 174411 (2014).
[25] P. Ho, A. K. Tan, S. Goolaup, A. G. Oyarce, M. Raju, L. Huang, A. Soumyanarayanan, and C. Panagopoulos, Phys. Rev. Applied **11**, 024064 (2019).
[26] T. Srivastava, Y. Sassi, F. Ajejas, A. Vecchiola, I. Ngouagnia, H. Hurdequint, K. Bouzehouane, N. Reyren, V. Cros, T. Devolder, et al., arXiv preprint arXiv:2111.11797 (2021).
[27] F. Büttner, B. Pfau, M. Böttcher, M. Schneider, G. Mercurio, C. M. Günther, P. Hessing, C. Klose, A. Wittmann, K. Gerlinger, et al., Nature materials **20**, 30 (2021).
[28] A. Bernand-Mantel, C. B. Muratov, and T. M. Simon, Phys. Rev. B **101**, 045416 (2020).
[29] G. Chen, A. Mascaraque, A. T. N'Diaye, and A. K. Schmid, Applied Physics Letters **106**, 242404 (2015), https://doi.org/10.1063/1.4922726.
[30] K. G. Rana, A. Finco, F. Fabre, S. Chouaieb, A. Haykal, L. D. Buda-Prejbeanu, O. Fruchart, S. Le Denmat, P. David, M. Belmeguenai, T. Denneulin, R. E. Dunin-Borkowski, G. Gaudin, V. Jacques, and O. Boulle, Phys. Rev. Applied **13**, 044079 (2020).
[31] N. K. Duong, M. Raju, A. Petrović, R. Tomasello, G. Finocchio, and C. Panagopoulos, Applied Physics Letters **114**, 072401 (2019).
[32] N. K. Duong, R. Tomasello, M. Raju, A. P. Petrović, S. Chiappini, G. Finocchio, and C. Panagopoulos, APL Materials **8** (2020), 10.1063/5.0022033, 111112.
[33] M. Ma, C. C. I. Ang, Y. Li, Z. Pan, W. Gan, W. S. Lew, and F. Ma, Journal of Applied Physics **127** (2020), 10.1063/5.0004432, 223901.
[34] S. Li, W. Kang, Y. Huang, X. Zhang, Y. Zhou, and W. Zhao, Nanotechnology **28**, 31LT01 (2017).
[35] K. M. Song, J.-S. Jeong, B. Pan, X. Zhang, J. Xia, S. Cha, T.-E. Park, K. Kim, S. Finizio, J. Raabe, et al., Nature Electronics **3**, 148 (2020).
[36] J. Grollier, D. Querlioz, K. Camsari, K. Everschor-Sitte, S. Fukami, and M. D. Stiles, Nature electronics **3**, 360 (2020).
[37] F. Ajejas, Y. Sassi, W. Legrand, S. Collin, J. P. Garcia, A. Thiaville, S. Pizzini, N. Reyren, V. Cros, and A. Fert, Physical Review Materials **6**, L071401 (2022).
[38] W. Legrand, Y. Sassi, F. Ajejas, S. Collin, L. Bocher, H. Jia, M. Hoffmann, B. Zimmermann, S. Blügel, N. Reyren, et al., Physical Review Materials **6**, 024408 (2022).
[39] W. Legrand, D. Maccariello, F. Ajejas, S. Collin, A. Vecchiola, K. Bouzehouane, N. Reyren, V. Cros, and A. Fert, Nature Materials **19**, 605 (2020).
[40] M. Belmeguenai, Y. Roussigné, S. M. Chérif, A. Stashkevich, T. Petrisor, M. Nasui, and M. S. Gabor, Journal of Physics D: Applied Physics **52**, 125002 (2019).
[41] L. Wang, C. Liu, N. Mehmood, G. Han, Y. Wang, X. Xu, C. Feng, Z. Hou, Y. Peng, X. Gao, and G. Yu, ACS Applied Materials & Interfaces **11**, 12098 (2019), https://doi.org/10.1021/acsami.9b00155.
[42] X. Wang, A. Cao, S. Li, J. Tang, A. Du, H. Cheng, Y. Sun, H. Du, X. Zhang, and W. Zhao, Phys. Rev. B **104**, 064421 (2021).
[43] S. Rohart and A. Thiaville, Phys. Rev. B **88**, 184422 (2013).
[44] M. Raju, A. P. Petrović, A. Yagil, K. S. Denisov, N. K. Duong, B. Göbel, E. Şaşıoğlu, O. M. Auslaender, I. Mertig, I. V. Rozhansky, and C. Panagopoulos, Nature Communications **12**, 2758 (2021).

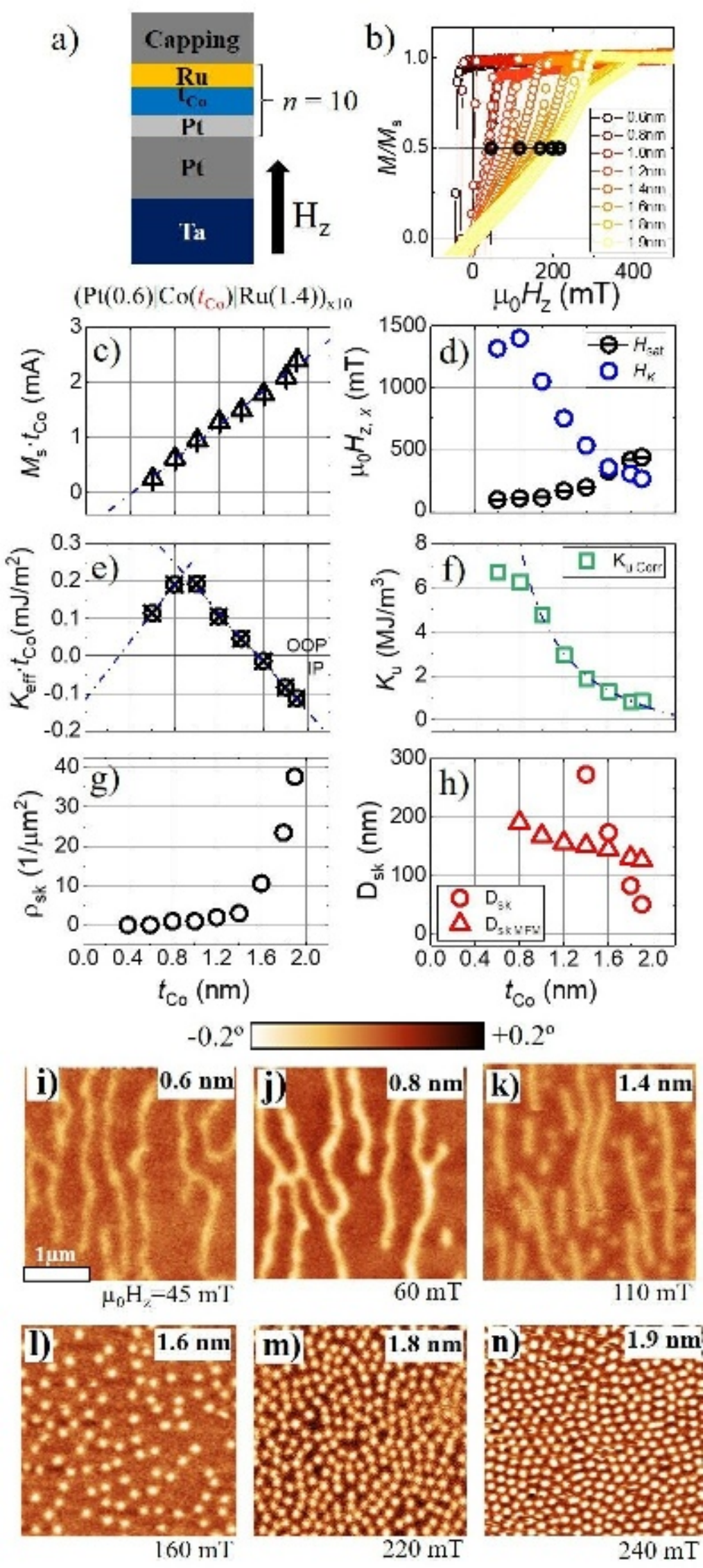
a)
Capping
Ru
t_{Co}
Pt
$n = 10$
Pt
Ta
H_z
b)
M/M_s
$\mu_0 H_z$ (mT)
0.6nm
0.8nm
1.0nm
1.2nm
1.4nm
1.6nm
1.8nm
1.9nm
$(Pt(0.6)|Co(t_{Co})|Ru(1.4))_{x10}$
c)
$M_s \cdot t_{Co}$ (mA)
d)
$\mu_0 H_{z,x}$ (mT)
H_{sat}
H_K
e)
$K_{eff} \cdot t_{Co}$ (mJ/m^2)
OOP
IP
f)
K_u (MJ/m^3)
$K_{u\,Corr}$
g)
ρ_{sk} (1/μm^2)
h)
D_{sk} (nm)
D_{sk}
$D_{sk\,MFM}$
t_{Co} (nm)
t_{Co} (nm)
-0.2°
+0.2°
i)
0.6 nm
1μm
$\mu_0 H_z$=45 mT
j)
0.8 nm
60 mT
k)
1.4 nm
110 mT
l)
1.6 nm
160 mT
m)
1.8 nm
220 mT
n)
1.9 nm
240 mT

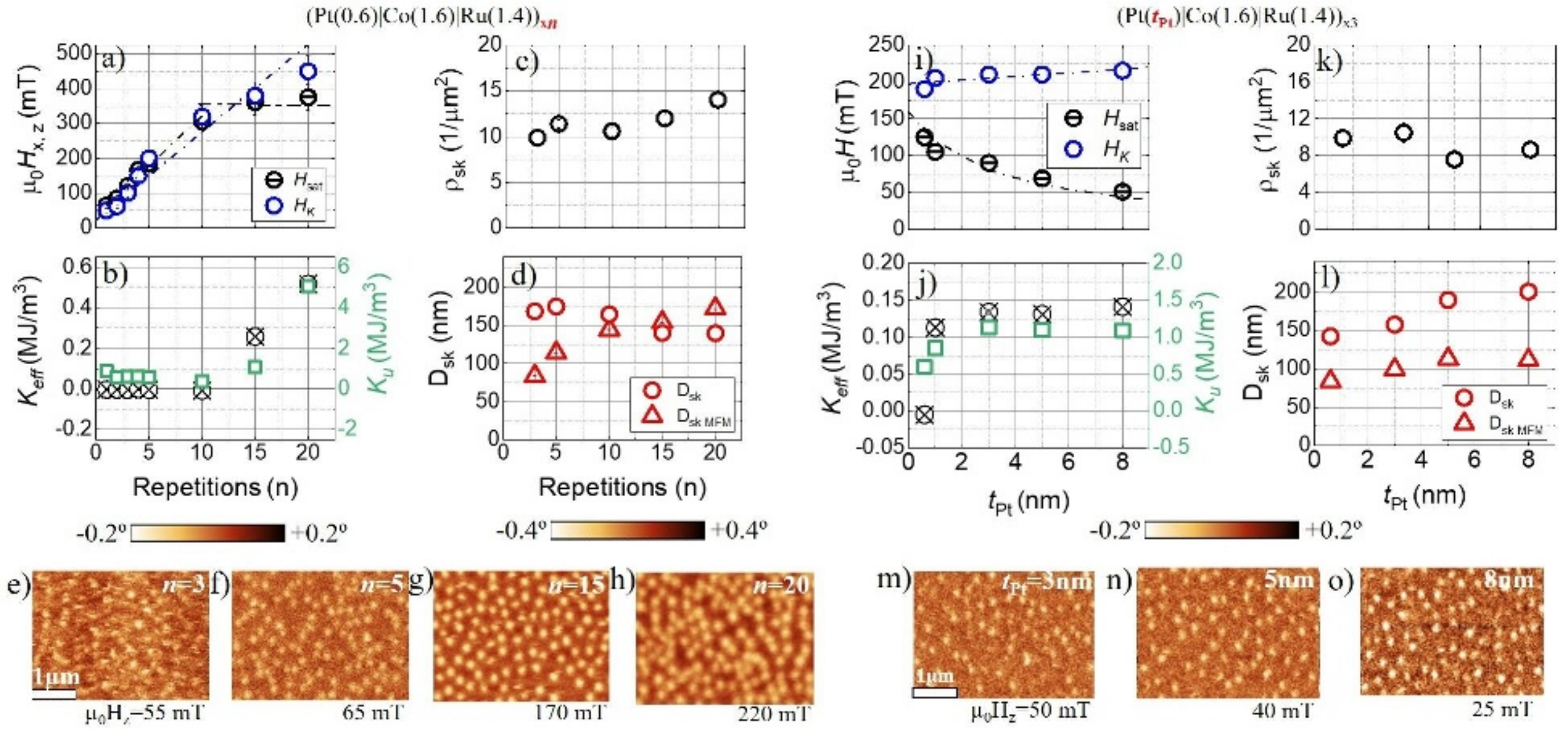
(Pt(0.6)|Co(1.6)|Ru(1.4))xn
(Pt(tPt)|Co(1.6)|Ru(1.4))x3
a)
b)
c)
d)
i)
j)
k)
l)
μ0Hx, z (mT)
Keff (MJ/m3)
Ku (MJ/m3)
ρsk (1/μm2)
Dsk (nm)
μ0H (mT)
Hsat
HK
Dsk
Dsk MFM
Repetitions (n)
tPt (nm)
-0.2°
+0.2°
-0.4°
+0.4°
e)
f)
g)
h)
m)
n)
o)
n=3
n=5
n=15
n=20
tPt=3nm
5nm
8nm
1μm
μ0Hz=55 mT
65 mT
170 mT
220 mT
μ0Hz=50 mT
40 mT
25 mT

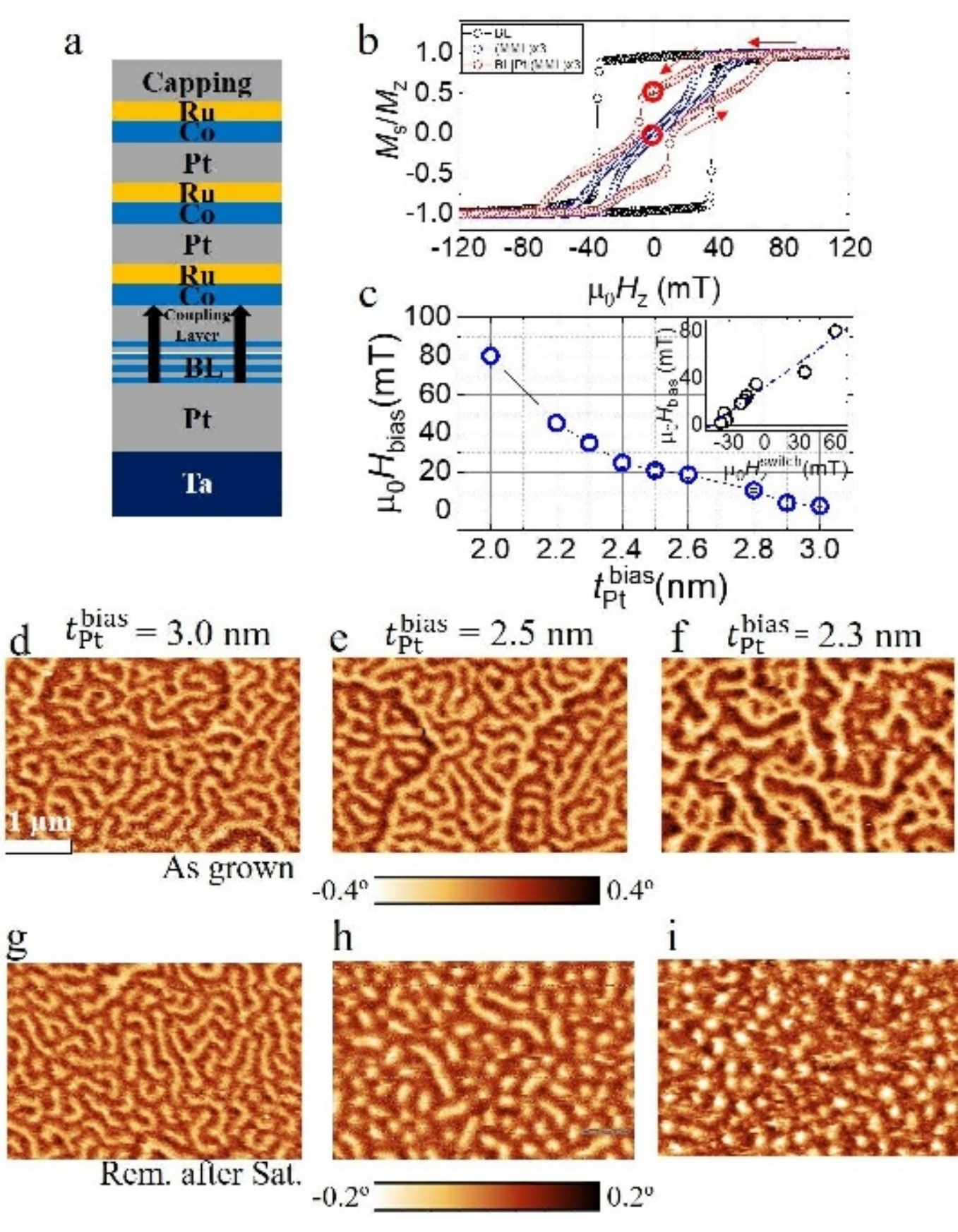
a
Capping
Ru
Co
Pt
Ru
Co
Pt
Ru
Co
Coupling Layer
BL
Pt
Ta
b
BL
(M/M) x3
BL [Pt (M/M) x3
M_s/M_z
1.0
0.5
0.0
-0.5
-1.0
-120 -80 -40 0 40 80 120
$\mu_0 H_z$ (mT)
c
$\mu_0 H_{bias}$(mT)
100
80
60
40
20
0
2.0 2.2 2.4 2.6 2.8 3.0
t_{Pt}^{bias}(nm)
$\mu_0 H_{bias}$ (mT)
80
40
0
-30 0 30 60
$\mu_0 H_c^{switch}$ (mT)
d t_{Pt}^{bias} = 3.0 nm
e t_{Pt}^{bias} = 2.5 nm
f t_{Pt}^{bias} = 2.3 nm
1 μm
As grown
-0.4°
0.4°
g
h
i
Rem. after Sat.
-0.2°
0.2°

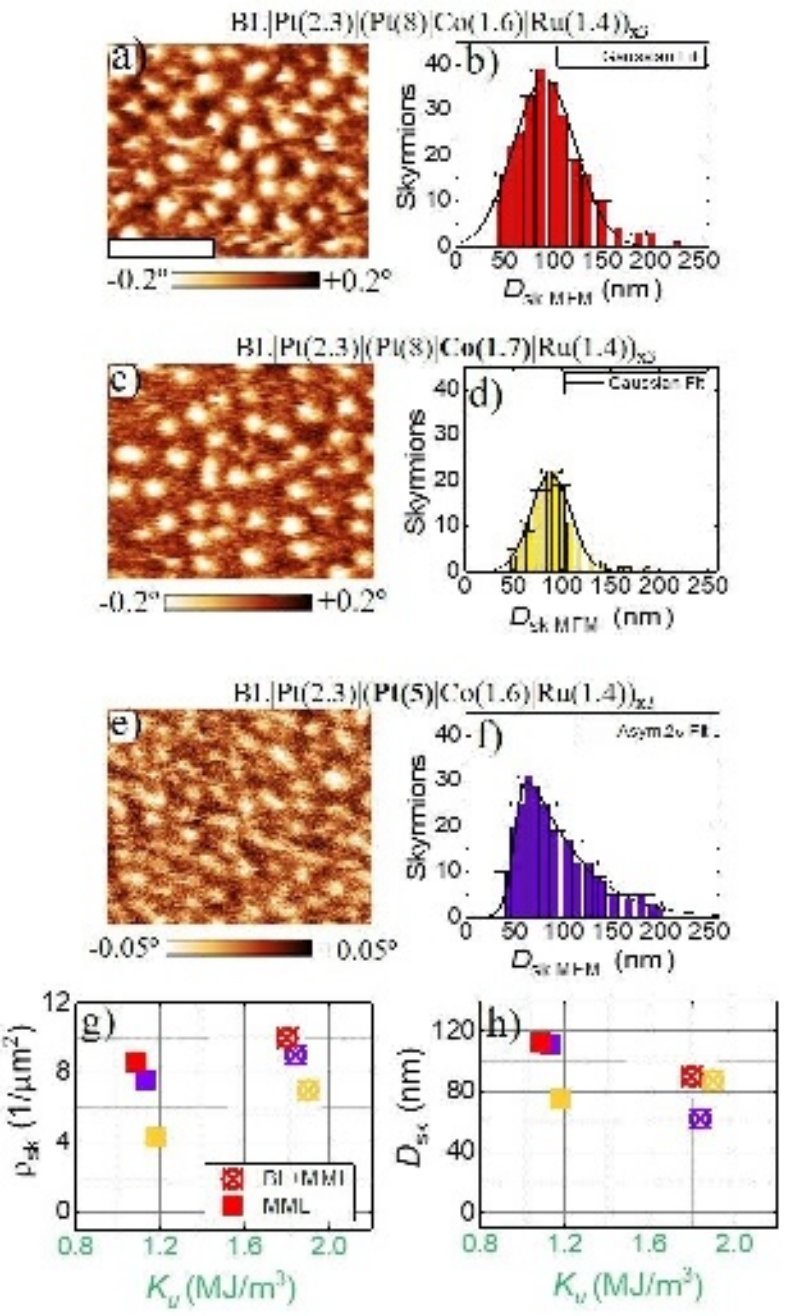
BL.|Pt(2.3)|(Pt(8)|Co(1.6)|Ru(1.4))x5
a)
-0.2°
+0.2°
b)
Skymions
$D_{sk\,MFM}$ (nm)
BL.|Pt(2.3)|(Pt(8)|Co(1.7)|Ru(1.4))x5
c)
-0.2°
+0.2°
d)
Skymions
$D_{sk\,MFM}$ (nm)
BL.|Pt(2.3)|(Pt(5)|Co(1.6)|Ru(1.4))x5
e)
-0.05°
0.05°
f)
Skymions
$D_{sk\,MFM}$ (nm)
g)
ρ_{sk} (1/μm²)
BL MML
ML
K_u (MJ/m³)
h)
D_{sk} (nm)
K_u (MJ/m³)